Fuel 353 (2023) 129185

Contents lists available at ScienceDirect

Fuel

journal homepage: www.elsevier.com/locate/fuel

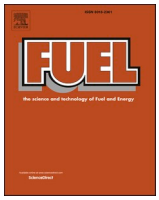

Full Length Article

Pyrolysis of food waste digestate residues for biochar: Pyrolytic properties, biochar characterization, and heavy metal behaviours

Yu Wang [a,b], Guangwei Yu [a,c,*], Shengyu Xie [d], Ruqing Jiang [a,b], Changjiang Li [a,e], Zhenjiao Xing [a]

[a] CAS Key Laboratory of Urban Pollutant Conversion, Institute of Urban Environment, Chinese Academy of Sciences, Xiamen 361021, Fujian, China
[b] University of Chinese Academy of Sciences, Beijing 101408, China
[c] Fujian Municipal Solid Waste Resource Recovery Technology Research Center, Xiamen 361021, Fujian, China
[d] School of Energy and Mechanical Engineering, Nanjing Normal University, 210023 Nanjing, China
[e] College of Life Sciences, Fujian Agriculture and Forestry University, Fuzhou 350002, Fujian, China

ARTICLE INFO

Keywords:
Food waste digestate residues
Pyrolysis
Thermal characteristics
Biochar
Heavy metals

ABSTRACT

The current work has examined the pyrolytic properties, product formation mechanisms, biochar properties, and heavy metal (HMs) safety of biochar during food waste digestate residue (DR) pyrolysis. The results have shown that DR pyrolysis proceeded in five stages. The kinetic model for Stages 1, 3 and 4 was the simple reaction order model, the one-dimensional diffusion model for Stage 2, and the three-dimensional (Jander) diffusion model for Stage 5. Based on thermogravimetric-Fourier transform infrared spectrometry (TG-FTIR) and pyrolysis–gas chromatography-mass spectrometry (Py-GCMS) analysis, the volatile components of the DR pyrolysis were mainly produced by the Maillard, decarboxylation, and deamination reactions as H_2O, CH_4, CO_2, CO, phenol, C═O (anhydride/ketone/aldehyde), C-O and NH_3. While there were six main components of the pyrolysis oil, that is, amines and amides, nitriles, N-hybrid compounds, oxides, and sulfides. Appropriate aromatic properties were observed in the prepared biochar, and the biochar obtained at a pyrolysis temperature of 700 °C had a relatively high specific surface area. The HMs results showed that the HMs in biochar obtained from DR pyrolysis at 400, 500, 600, 700, and 800 °C were predominantly in the oxidizable and residual fractions. The toxicity characteristic leaching procedure (TCLP) tests and the potential ecological risk indices for HMs have indicated a high safety profile for biochar. This work has elucidated the formation process of DR pyrolysis products and the physicochemical properties and safety of biochar. It has also provided an outlet for the application of biochar, which provides a strong contribution to promoting resource use of DR.

1. Introduction

With increasing consumption and rapid development in the catering industry, and especially in the takeaway industry in China, the amount of food waste (FW) generated has also increased yearly. Annual production of FW has increased from 94.75 million tons in 2015 to 121.03 million tons in 2019 [1]. This trend is expected to show continued growth, including a decline in growth rates in early 2020 from the impacts of Covid-19. Traditional treatment methods, including incineration, landfilling, and composting, are likely to cause adverse effects on the surrounding environment [2,3]. As a renewable energy production and waste treatment technology [4,5], anaerobic digestion (AD) has become a mainstream technology for FW treatment with its relatively low cost and high level of efficiency [6]. However, while anaerobic fermentation of food waste generates high levels of secondary energy, treatment and disposal of the by-product digestate residues (DR) is becoming an increasing concern [7]. DR production in China reached 14.43 million tons by the end of 2020 [8]. The high water, oil, and salt content and high viscosity of DR, as well as the potential presence of harmful substances such as pathogenic microorganisms, polychlorinated bromides (PCBs), polycyclic aromatic hydrocarbons (PAHs), chlorinated paraffin, phenolic compounds, and phthalates mean that its safe disposal is vital.

The most common treatment and disposal protocols for DR include

* Corresponding author at: CAS Key Laboratory of Urban Pollutant Conversion, Institute of Urban Environment, Chinese Academy of Sciences, Xiamen 361021, Fujian, China.
E-mail address: gwyu@iue.ac.cn (G. Yu).

https://doi.org/10.1016/j.fuel.2023.129185
Received 20 February 2023; Received in revised form 3 July 2023; Accepted 5 July 2023
Available online 14 July 2023

Table 1
Basic parameters of DR (Dry basis).

Sample	Proximate analysis (wt.%)					Elementals analysis (wt.%)				
	Ash	VM[a]	FC[b]	N	C	H	S	O[c]	H/C	N/C
DR	48.05	49.41	2.54	3.49	22.72	3.22	0.39	22.13	1.70	0.13
	Na	Mg	Al	Si	P	Cl	K	Ca		
DR	0.43	1.34	0.68	1.02	2.07	0.78	0.23	26.10		

[a] VM, Volatile matter.
[b] FC, Fixed carbon.
[c] O, By difference, O = 100 − (C + H + N + S + Ash).

fertilizer, sanitary landfill, aerobic composting, and incineration. Although the Chinese government has introduced some policies related to the use of DR fertilizer to provide an outlet for its sustainable use, compound fertilizer companies are more inclined to use higher-quality organic raw materials because of the poor quality and impurities of DR. Meanwhile, approximately 15% of the organic matter is consumed during the DR fermentation process. Some nutrients are lost during the solid–liquid separation process, which further hinders the use of DR fertilizer [9]. Traditional sanitary landfill and aerobic composting have the disadvantages of polluting groundwater, contaminating soil, producing foul odors, and having long cycles [10,11]. Meanwhile, incineration can generate ashes and has risks from emitting particulate and gaseous pollutants [12]. In recent years, thermal conversions such as pyrolysis and hydrothermal treatment have been widely used for various biomass and solid wastes because of their ability to achieve substantial reduction, harmlessness, and resource recovery under high-pressure, high-temperature conditions. For organic solid waste of higher quality, the process of hydrothermal combined with anaerobic fermentation can fully realize the high-value utilization[13], while preparation of solid fuels through hydrothermal treatment is unlikely to have an advantage in terms of product competition because of the low quality of DR. Pyrolysis technology is more thorough in reducing and eliminating organic pollutants than hydrothermal technology, and the prepared biochar has a wide range of application prospects. For DR, the preparation of digestate biochar (DRC) by pyrolysis can reduce the environmental impact and produce functionalized biochar with different applications, i.e., soil amendment or adsorbent materials. This product has more extensive market application [14]. DR is more affordable and contains high levels of nitrogen, phosphorus, potassium, and other effective elements compared with other conventional biomass, which are further enriched during the pyrolysis process. This means that it can potentially increase crop yields after initial treatment and fertilization [15,16]. Given that DR contains calcium carbonate, there is no need to add additional activators during the pyrolysis process to expand the pores and enrich the pore structure. The high nitrogen content in DR may lead to the formation of more nitrogen-containing compounds in the bio-oil. These can have various applications as biofuels or chemicals. However, to date, more research has been focused on improving the anaerobic digestion effect of FW and the land use of DR [17,18]. Meanwhile, there is still insufficient research on the pyrolysis carbonization and pyrolysis behaviour of DR. Kinetics have been extensively to various biomass pyrolysis and mutual co-pyrolysis. However, to date, it has not yet been systematically linked to DR pyrolysis. DR pyrolysis involves many complex reaction pathways, and the temperatures, residue time, DR composition, and other factors can affect the pyrolysis process to the extent that it affects the distribution and characteristics of products. Understanding these pyrolysis parameters and characteristics is of considerable importance in the resource use of DR and DRC. There are also safety issues with some heavy metals (HMs) in DR. However, the HMs safety in the pyrolysis product DRC has been less explored. This has also prompted the need to pay attention to the risk of HMs in the follow-up use of DRC.

Therefore in this study, the pyrolysis characteristics and kinetics of DR were systematically studied using a thermogravimetric analyzer with three different heating rates. The kinetic parameters of the DR pyrolysis process were calculated using the Flynn–Wall–Ozawa (FWO), Kissinger–Akahira–Sunose (KAS), and integral master plot methods. Thermogravimetric-Fourier transform infrared spectrometry (TG-FTIR) and pyrolysis–gas chromatography-mass spectrometry (PY-GCMS) have also shown the mechanisms of product formation in the gas and liquid phases. To ensure the safety of biochar during application, the European Community Bureau of Reference (BCR) continuous extraction method and toxicity characteristic leaching procedure (TCLP) was used to evaluate the potential ecological risks of DR and DRCs. The findings of this study may offer potential solutions for the reduction, non-hazardous, and resourceful recycling of DR.

2. Materials and methods

2.1. Raw material

DR with an initial water content of 80.27% was collected from a food waste anaerobic fermentation treatment plant in Dongguan, Guangdong province. Before the experiments, DR was dried in an oven to constant weight at 105 °C for 48 h and then ground into particles smaller than 0.15 mm for further analysis. The essential characteristics of DR are listed in Table 1.

2.2. Pyrolysis characteristics and kinetic analysis

A thermogravimetric analyzer (STA2500, NETZSCH, Germany) was used to analyze the pyrolytic properties of DR. An excessive mass of DR can significantly affect the effectiveness of heat and mass transfer between particles. To eliminate this effect, we set the initial group of DR to below 10 mg. We then held it for 10 min after heating it from 30 °C to 850 °C at the rates of 20, 30 and 40 °C/min, respectively. The flow rate of the protective gas N_2 was set to 100 mL/min. Division of the overlapping parts, initial decomposition temperature, termination decomposition temperature, and the peak temperature of each stage of DR pyrolysis were identified according to the Fraser–Suzuki deconvolution method recommended by the International Confederation for Thermal Analysis and Calorimetry (ICTAC) [19]. Devolatilization Index D that can be evaluated for DR pyrolysis performance can be obtained using equation Eq. (1) and (2) [20]:

$$D = \frac{(-DTG_{max}) \times (-DTG_{average})}{T_i \times T_{peak} \times \Delta T_{1/2}} \quad (1)$$

$$D = \sum_i \Delta W_i \times Di \quad (2)$$

where T_i and T_p are initial decompositions and peak temperatures, °C; $\Delta T_{1/2}$ is the temperature range at the half value of $-DTG_m$, °C; ΔW_i is the weight loss of each stage as a percentage of the total weight loss; D_i is Devolatilization Index D for each stage of DR pyrolysis. In general, a higher Index D means a more effective DR pyrolysis performance.

2.2.1. Kinetic analysis

DR pyrolysis involves many complex chemical and physical processes. However, each process stage can be modeled mathematically. Given that DR also fits the non-homogeneous reaction system and non-isothermal conditions in the pyrolysis of solid fuels, it can be described using Eq. (3) [21]:

$$\frac{d\alpha}{dT} = k(T)f(\alpha) \tag{3}$$

where $d\alpha/dT$, α, $k(T)$ and $f(\alpha)$ are the degradation rate, the conversion degree, the reaction rate constant, and the differential mechanism function, respectively.

Eq. (4) is obtained by replacing $k(T)$ with the Arrhenius equation [22]:

$$\frac{d(\alpha)}{f(\alpha)} = \frac{A}{\beta} exp\left(-\frac{E}{RT}\right)dT \tag{4}$$

where T, A, E, R, and β are the absolute temperature (K), the pre-exponential factor (1/min), the activation energy (kJ/mol), the ideal gas constant (8.314 J/(mol·K)), and the heating rate (K/min).

The α can be calculated using Eq. (5) [23]:

$$\alpha = \frac{m_0 - m_i}{m_0 - m_u} \tag{5}$$

where m_o, m_i, and m_u are the initial, instantaneous, and ultimate masses of each stage of DR, respectively, mg.

Eq. (6) can be obtained by integrating Eq. (4):

$$G(\alpha) = \int_0^{\alpha} \frac{d\alpha}{f(\alpha)} = \frac{A}{\beta}\int_{T_0}^{T} exp\left(-\frac{E}{RT}\right)dT \tag{6}$$

where $G(\alpha)$ is the integrated form of $f(\alpha)$ and T_0 is the initial temperature at each stage of the pyrolysis reaction.

2.2.2. Calculation of activation energy (E)

Model-free methods are widely used in studying biomass pyrolysis because they can describe the kinetic triplet, which includes A, E, and $f(\alpha)$, without assuming a reaction model. In this study, the FWO and KAS methods were used, as recommended by the ICTAC Kinetics Committee, to calculate the E values [24]. The two methods can be expressed as follows:

$$ln\beta = ln\frac{0.0048AE}{RG(\alpha)} - 1.0516\frac{E}{RT}(FWO) \tag{7}$$

$$ln\left(\frac{\beta}{T^2}\right) = ln\left(\frac{AE}{EG(\alpha)}\right) - \frac{E}{RT}(KAS) \tag{8}$$

For a given α of which the range was from 0.2 to 0.8 with a step of 0.05, the values of E can be obtained from the slopes of the regression lines by plotting lnβ versus 1/T (FWO) and ln (β/T^2) versus 1/T (KAS), respectively.

2.2.3. Integral master plot method

Given the prolonged decomposition rate of DR at ambient temperature T_0, Eq. (6) can be described by a master plot method as follows:

$$G(\alpha) = \int_{T_0}^{T}\frac{A}{\beta}exp\left(-\frac{E}{RT}\right)dT \approx \int_0^{T}\frac{A}{\beta}exp\left(-\frac{E}{RT}\right)dT = \frac{AE}{\beta R}P(u_\alpha) \tag{9}$$

where $u_\alpha = E/RT$, E is the average of the activation energies calculated using the FWO and KAS methods, T is the temperature corresponding to a particular α, and $P(u_\alpha)$ is the temperature integral. Given that there is no analytical solution for $P(u_\alpha)$, the Tang–Liu–Zhang–Wang–Wang approximate expression [25], an empirical equation, was used here to calculate $P(u_\alpha)$ with a deviation of less than 0.1% when u greater than 14.

$$P(u_\alpha) = \frac{exp(-u_\alpha)}{u_\alpha \times (1.00198882u_\alpha + 1.87391198)} \tag{10}$$

For each single-step reaction, $f(\alpha)$, E and A are constants.

The kinetic triplets ($f(\alpha)$, E and A) are constant for each step reaction. A suitable mechanism function can then be used to simulate the TG data by obtaining the value of E, which the previous equation can be used to calculate. Here, $\alpha = 0.5$ was selected as a reference, then Eq. (10) can be converted into Eq. (11) as follows:

$$G(0.5) = \frac{AE}{\beta R}P(u_{0.5}) \tag{11}$$

The integral master-plot equation can be obtained by dividing Eq. (9) by Eq. (11).

$$\frac{G(\alpha)}{G(0.5)} = \frac{P_{(u)}}{P(u_{0.5})} \tag{12}$$

Based on ICTAC Kinetics Committee recommendations [26], the 15 standard thermal degradation reaction models $G(\alpha)$ are listed in Table S1 of Electronic Supplementary Information (ESI). A series of theoretical master-plots and experimental master-plots can be obtained by plotting $G(\alpha)/G(0.5)$ versus α and $P(u_\alpha)/P(u_{0.5})$ versus α on the left and right hand of Eq. (12). For a given determined α, the most appropriate process for each stage of DR pyrolysis was determined by finding the closest model to the experimental master plots.

2.3. Pyrolysis experiments

The DRCs preparation processes were conducted in a fixed bed reactor (Fig. S1). Approximately 20 g of DR was placed into matched quartz pyrolysis tubes. To ensure that the entire process was conducted under oxygen-free conditions, nitrogen with a purity of 99.99% was introduced 10 min before the warming procedure commenced and was maintained at 100 mL/min. The reactor was heated from 30 °C to 400, 500, 600, 700 and 800 °C, respectively, at a rate of 20 °C/min and maintained for 45 min after reaching the target temperature. After cooling to the ambient temperature, the biochar was ground and filtered through a 100-mesh standard sieve. The biochar samples obtained were named DRC-400, DRC-500, DRC-600, DRC-700, and DRC-800. These have been collectively referred to as DRCs.

2.4. Experimental analysis method

The proximate analysis included ash, volatile matter (VM), and fixed carbon (FC) of DR and DRCs referred to as the national standard GB/T 28731–2012. Elemental analysis (C, N, H, and S) was conducted using an elemental analyzer (Elementar Vario EL cube, Ellimenta, Germany), where the O content was calculated according to the difference (O = 100 – Ash – C – H – N – S). The inorganic mineral contents (Na, Mg, Al, Si, P, Cl, K, Ca) were determined using X-ray fluorescence spectrometry (XRF, Axios mAX, PANalytical Axios-mAX, Netherlands). The surface functional groups were determined using Fourier transform infrared spectrometry (FTIR, iS10, Thermo Fisher Scientific, America). A surface area and porosity analyzer was used to examine the surface area and pore structure (ASAP2020, Micromeritics, America). Prior to the adsorption measurements being conducted, the DR and DRCs samples were vented for 2 h at 200 °C under a vacuum.

To follow the production of the main products during the DR pyrolysis, TG-FTIR experiments were conducted at 20 °C/min. The oil phase was obtained by purging with 500 mL/L of high-purity Ar. The condensable gas fraction was removed with acetone, while the non-condensable gas phase product was analyzed online using FTIR spectroscopy. The program was set to obtain FTIR spectra at eight scans per sample over a temperature range of 30–800 °C with a resolution of 4 cm^{-1}. Py-GCMS was conducted with pure helium as the carrier gas for

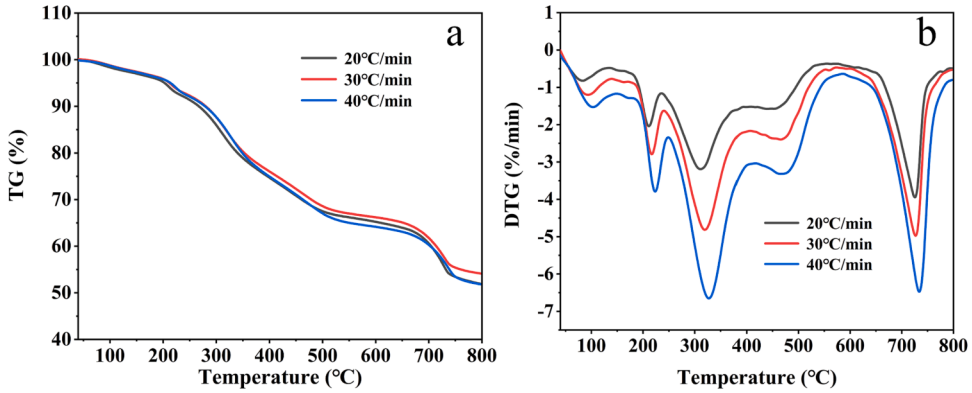

Fig. 1. TG (a) and DTG (b) curves of DR pyrolysis at three different heating rates.

Table 2
Pyrolysis parameters and Devolatilization Index D of DR under three different heating rates.

	β (°C/min)	T_i (°C)	T_p (°C)	$-DTG_m$ (%/min)	T_u (°C)	$-DTG_a$ (%/min)	$\Delta T_{1/2}$ (°C)	ΔW (%)	D_i (%^{2}/(K^3·min^2))	D (%^{2}/(K^3·min^2))
Stage1	20	40	83	0.82	134	0.59	31	5.28	1.40×10^{-7}	$D_{20} = 2.16 \times 10^{-6}$; $D_{30} = 3.94 \times 10^{-6}$; $D_{40} = 7.22 \times 10^{-6}$.
	30	40	92	1.20	139	0.84	35	5.10	2.50×10^{-7}	
	40	40	102	1.53	148	1.07	39	5.10	3.57×10^{-7}	
Stage2	20	134	211	2.04	236	1.02	23	10.98	5.95×10^{-7}	
	30	139	216	2.79	241	1.44	23	10.57	1.14×10^{-6}	
	40	148	223	3.79	248	2.11	24	10.67	2.14×10^{-6}	
Stage3	20	236	311	3.19	394	2.15	43	35.98	8.72×10^{-7}	
	30	241	319	4.81	406	3.11	45	36.81	1.79×10^{-6}	
	40	248	327	6.65	416	4.36	46	37.89	3.35×10^{-6}	
Stage4	20	394	439	1.58	570	1.06	85	19.72	8.80×10^{-8}	
	30	406	465	2.40	573	1.60	82	19.15	2.02×10^{-7}	
	40	416	465	3.32	585	2.19	83	19.07	3.79×10^{-7}	
Stage5	20	570	725	3.95	775	1.29	35	28.04	4.66×10^{-7}	
	30	573	726	4.97	848	1.44	41	28.37	5.58×10^{-7}	
	40	585	733	6.47	849	2.05	42	27.28	9.99×10^{-7}	

12 s at 800 °C for pyrolysis. The volatile products were separated using an HP-5MS capillary column (5% phenyl-95% dimethylpolysiloxane, 30 m × 0.32 mm × 0.25 μm). Mass spectral data were obtained in electron ionization mode at 70 eV. Compound yields were calculated from standard solution calibration derived from the National Institute of Standards and Technology (NIST) library database GC–MS spectra.

2.5. Heavy metal detection and analysis methods

According to the three-step extraction procedure formulated using the BCR continuous extraction method, HMs have divided into four fractions. The F1 fraction is the acid-soluble fraction, mainly adsorbed on the surface of particles or in the form of carbonates, and is susceptible to the type of ions in the water column and their adsorption and desorption. The F2 fraction is the reducible fraction, mainly in the form of iron and manganese oxides combined in an unstable form under anoxic or anaerobic conditions. The F3 fraction is the oxidizable fraction, the form in which heavy metals are combined with organic matter and sulphides. It can be degraded under certain conditions to become bioavailable. The F4 fraction is the residual fraction, that is, the form in which heavy metals are bound to silicate minerals and crystalline Fe-Mg oxides. The F4 fraction is relatively stable and difficult to activate or use [27]. The specific extraction process is shown in Fig. S2. The final leaching solutions were determined using inductively coupled plasma mass spectrometry (ICP-MS, Agilent Technologies, 7500CX, Santa Clara, CA). The leaching toxicity of HMs used the Toxicity Characteristic Leaching Procedure method developed by the United States Environmental Protection Agency (EPA. US). 1 g sample was extracted with 20 mL of 0.1 mol/L acetic acid solution (pH = 2.88), then centrifuged, filtered, and leached for analysis using ICP-MS.

The HMs potential ecological risk index was used to evaluate the potential pollution risk of solid waste, which can be obtained using Eq. (13) [28].

$$RI = \sum E_r = \sum (T_f \cdot C_f) = \sum \left(T_f \cdot \frac{W_s}{W_n} \right) \quad (13)$$

where C_f is the single metal pollution coefficient, Ws is the total concentration of F1, F2, and F3, and W_n is the concentration of F4. T_f is the individual HM toxicity response factor of which eight typical heavy metals are: Cd (30) > As (10) > Ni (6) > Cu (5) = Pb (5) > Cr (2) > Mn (1) = Zn (1) [29]. E_r is a single potential ecological risk index, RI is potential ecological risk index of DR or DRCs. Indicators and thresholds for the potential ecological risk of heavy metals are shown in Table S2.

3. Results and discussion

3.1. Thermogravimetric analyses of DR

The TG and DTG curves of DR pyrolysis in the N_2 atmosphere under three heating rates are shown in Fig. 1. Pyrolysis of DR could be divided into five stages corresponding to the five more pronounced weightless peaks in the DTG diagram as shown in Fig. 1(b). Stage 1 was from 40 °C to 148 °C with a weight loss of 2.5 wt%, and Stage 2 was from 148 °C to 248 °C with a weight loss of 5.2 wt%. These were caused by water evaporation and light volatiles decomposing, which were also reported by Hu et al., but at slightly lower temperatures than in the present study [30]. Extending from 248 °C to 416 °C with a weight loss of up to 18.5%, Stage 3 was the main stage of DR pyrolysis because of the decomposition of hemicellulose, cellulose and extracts including protein, starch,

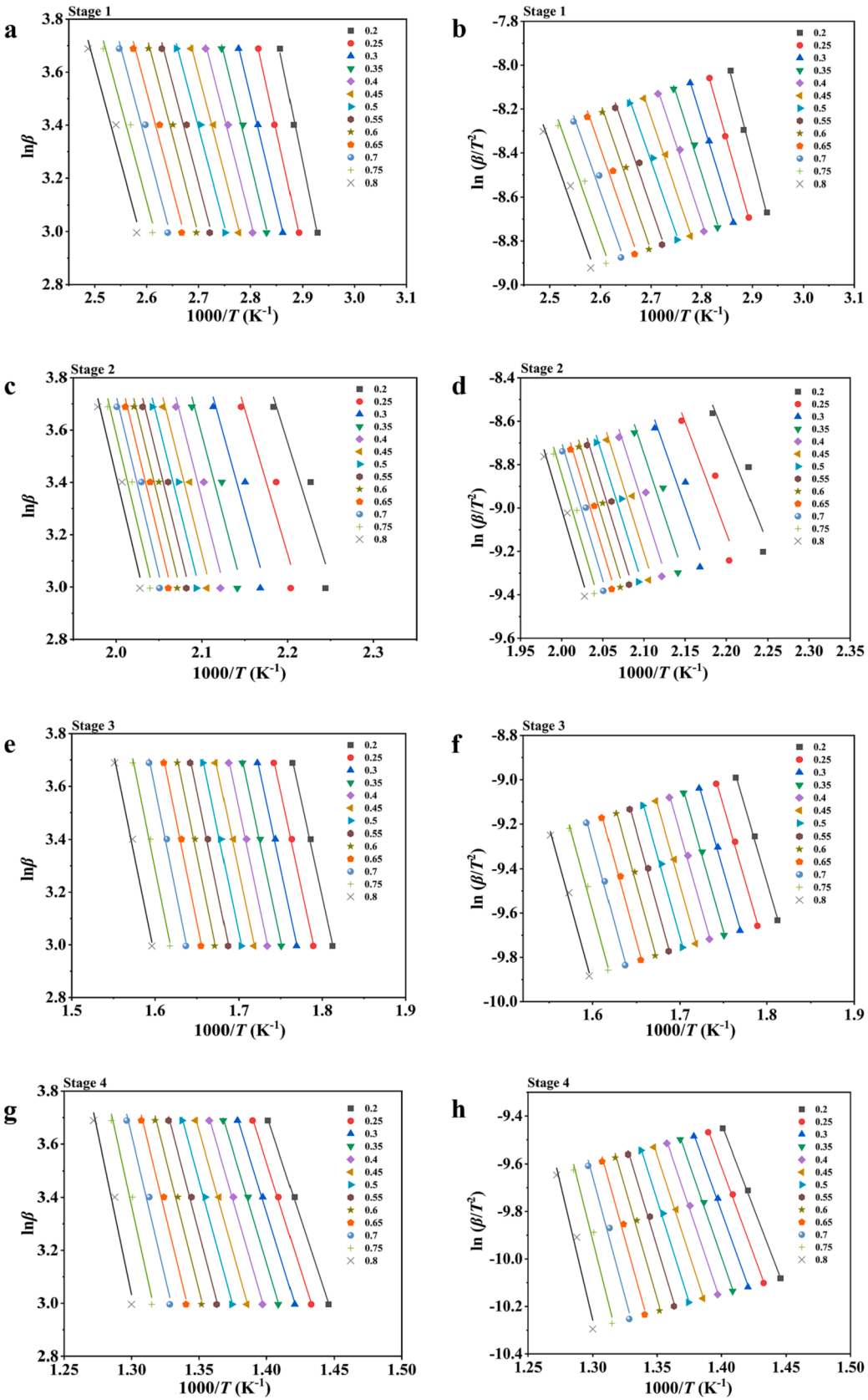

Fig. 2. Kinetic plots for the five sub-stages according to FWO and KAS.

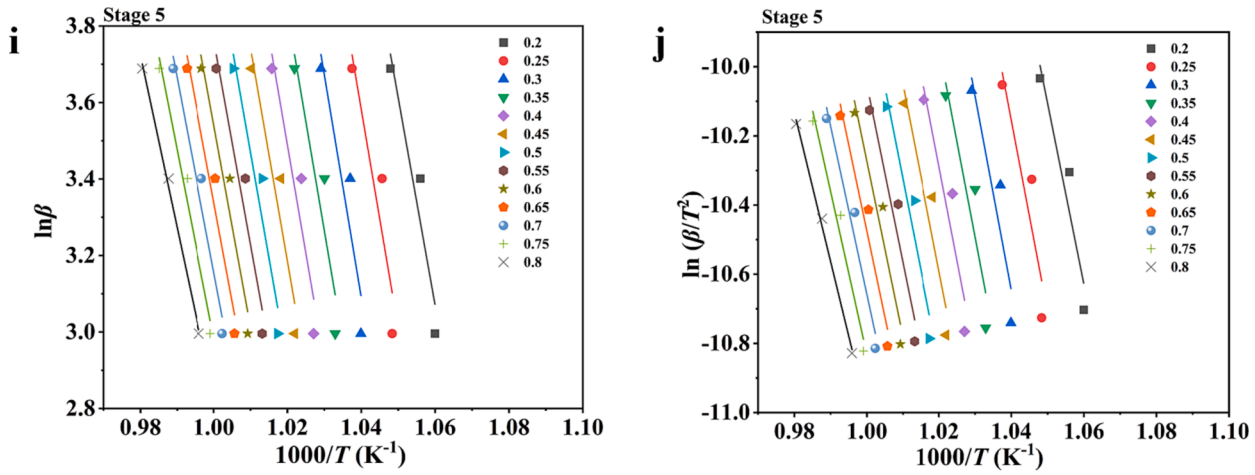

Fig. 2. (*continued*).

carbohydrate, and aliphatic [31]. Similar results were found in the study of penicillin fermentation residue by Wang et al. with a slightly larger temperature range, which was attributed to the greater abundance of organic matter in the penicillin fermentation residue [32]. Stage 4 was from 416 °C to 585 °C with a weight loss of 9.3 wt%, which was predominantly associated with macromolecular substances and lignin decomposition. It was reported that the pyrolysis of hemicellulose, cellulose and lignin occurred mainly at 200 to 300 °C, 300 to 400 °C and 200 °C until the end of the pyrolysis process, respectively [33]. At this stage, it was often accompanied by secondary reactions such as repolymerization and condensation to form chars [34]. Stage 5 corresponds to the decomposition of calcium carbonate resulting from the decomposition of organic calcium compounds in the temperature range of 585–844 °C, slightly different from the 630–680 °C reported by Liu et al [35]. The limitations of heat and mass transfer made the TG and DTG curves move to the higher temperature on the right as the heating rate increased.

Table 2 shows the pyrolysis parameters and Devolatilization Index D of DR pyrolysis at different heating rates. The initial temperature (T_i), peak temperature (T_p), and ultimate temperature (T_u) in the five stages all increased with the increase in pyrolysis rate. The DTG curve also tended to shift to the right, which did not change the thermal profile of decomposition. The maximum weight loss rate ($-DTG_m$) for Stages 1, 2, 3, 4, and 5 increased from 0.82, 2.04, 3.19, 1.58, and 3.95 at 20 °C/min to 1.53, 3.79, 6.65 3.32, and 6.47 wt.%/min at 40 °C/min, respectively. This phenomenon can be attributed to a significant temperature difference between the inside and outside of the DR particles because of the poor thermal conductivity of DR, and volatiles will be released faster at higher heating rates. Devolatilization Index D, one of the parameters for evaluating DR pyrolysis performance, also increased with the increase in heating rate, and the values of Index D at 20, 30, and 40 °C/min was 2.16×10^{-6}, 3.94×10^{-6}, 7.22×10^{-6} $\%^2/(K^3 \cdot min^2)$, respectively. In conclusion, a higher heating rate can improve the pyrolysis performance of DR.

3.2. Pyrolysis kinetics analysis of DR

The least-square method was used to calculate the apparent activation energy (E_α) according to the FWO and KAS method. In this study, to more effectively show the variation in E_α values for DR, the corresponding characteristic transformation (α) ranging from 0.2 to 0.8 with an interval of 0.05 was used for each stage. As shown in Fig. 2, linear relationships were obtained using the plots of $\ln\beta$ (FWO) and $\ln[\beta/T^2]$ (KAS) versus $1/T$ at the given α. The correlation coefficients R^2 of the five stages were from 0.9602 to 0.9996, 0.8686–0.9621, 0.9925–0.9970, 0.9684–0.9991, and 0.8561–0.9968 at five different stages, respectively. Given that the energy required for different reactions in the DR pyrolysis process was different, the E values constantly changed with the degree of conversion. The E values of Stage 1 and Stage 5 decreased with the addition of α, while those of Stage 2, 3, and 4 were the opposite. The E values obtained using the two methods were almost the same, which indicated the data calculated was reliable. The E values calculated with FWO and KAS were 61.71 and 58.71 kJ/mol for the Stage 1 and 101.5 and 98.8 kJ/mol for Stage 2, which are similar to the 64.88 ~ 92.02 kJ/mol reported by Liu et al. [35]. In Stage 3, the E values increased to 120.2 and 116.6 kJ/mol, respectively, lower than the E values of 168.85 kJ/mol for organics, according to Wang et al. [32]. This may be because the pyrolysis of DR at this stage was also involved in the degradation of low-energy hemicelluloses and small molecules. In Stage 4, the E values of 151.7 and 151.0 kJ/mol were lower than those of 236.7 kJ/mol for pure lignin, which was attributed to the more complex composition of DR, containing not only lignin but also other macromolecules [36]. The E values calculated in Stage 5 were the highest, reaching 424.4 and 429.2 kJ/mol using the two methods. The activation energy reflects the difficulty of the DR pyrolysis reaction, as explained in Section 3.1. During DR pyrolysis, decomposition of the organic calcine often required higher energy. To use the DR more effectively, we can control the pyrolysis temperature according to the product requirements to achieve the strongest energy-saving effect.

3.3. Reaction model from the master plots

The integral master plot method used the average activation energy for each stage calculated using the two methods in Section 3.3.2. The average activation energy values for the five stages were 60.21, 100.15, 118.40, 151.39, and 426.82 kJ/mol, respectively. The reaction kinetics of DR pyrolysis process could be expressed once the necessary pre-exponential factor (A), the model, and the order of reaction (n) had been calculated. As shown in Fig. 3 (a, c, e, g, and i), the $P(u)/P(u_{0.5})$ plots for the different heating rates at each stage were almost the same. This indicated that the kinetic degradation mechanism would not change excessively with the heating rate. Therefore, the kinetics of each stage of DR pyrolysis could be described using a single kinetic model. The experimental master plot of the heating rate with 30 °C/min was used as the research object to compare with the theoretical master plots to find the most likely dynamic model, as shown in Fig. 3 (b, d, f, h, and j).

Comparing Stage 1 and Stage 4 with F2 of the theoretical master plots, that is, a simple reaction order model, it was found that the two had a higher degree of matching. This result was also in line with the findings of Cai et al. [37], who found that F2 could fit the decomposition process of cellulose and lignin effectively. Meanwhile, Stage 2 was close

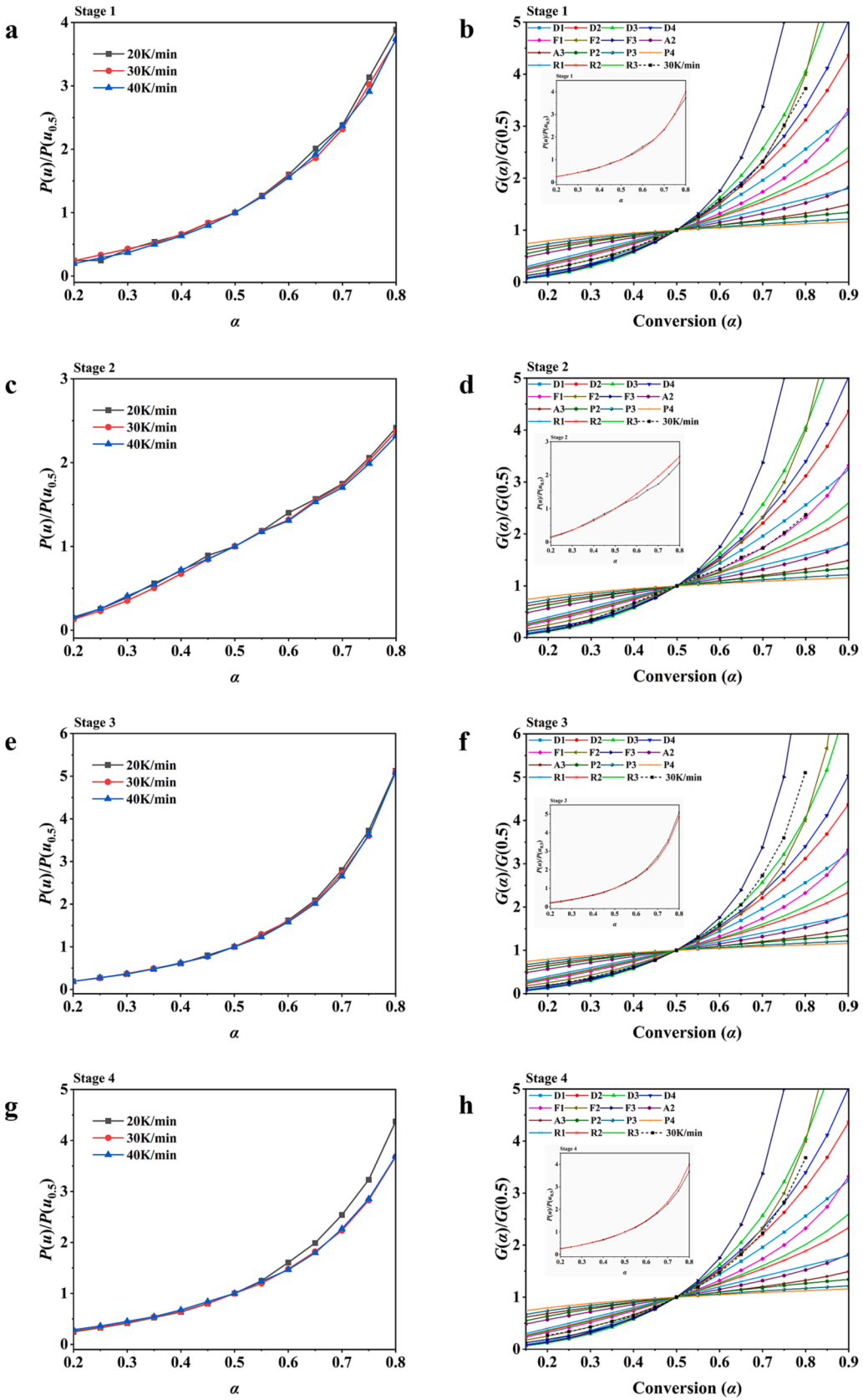

Fig. 3. Experimental master plots of $P(u_\alpha)/P(u_{0.5})$ vs. α for each stage of DR pyrolysis.

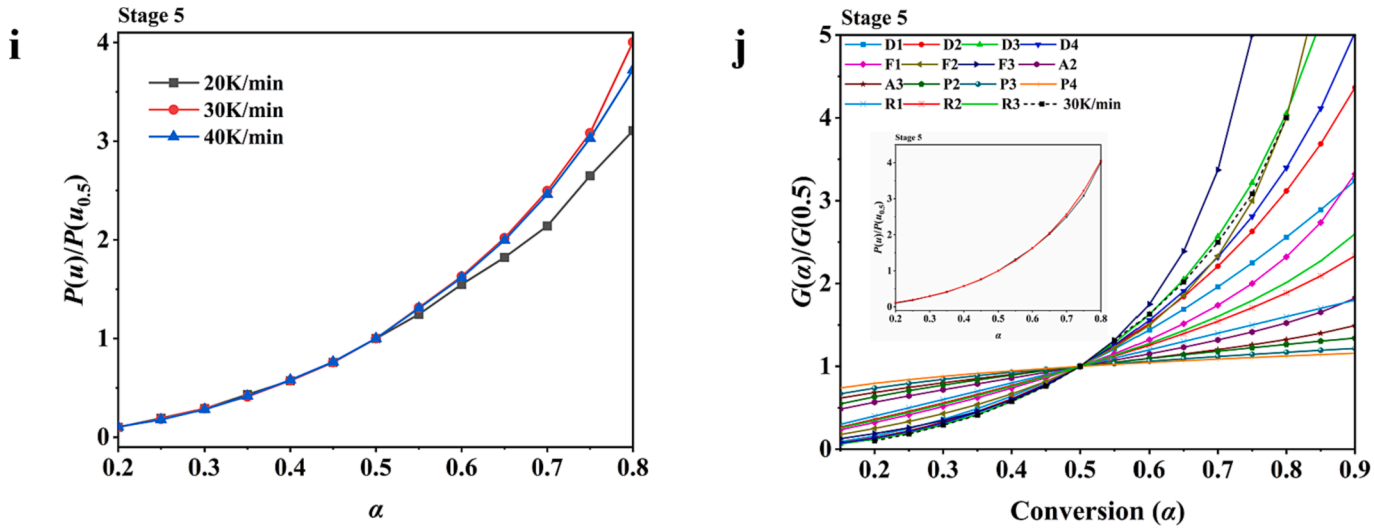

Fig. 3. (*continued*).

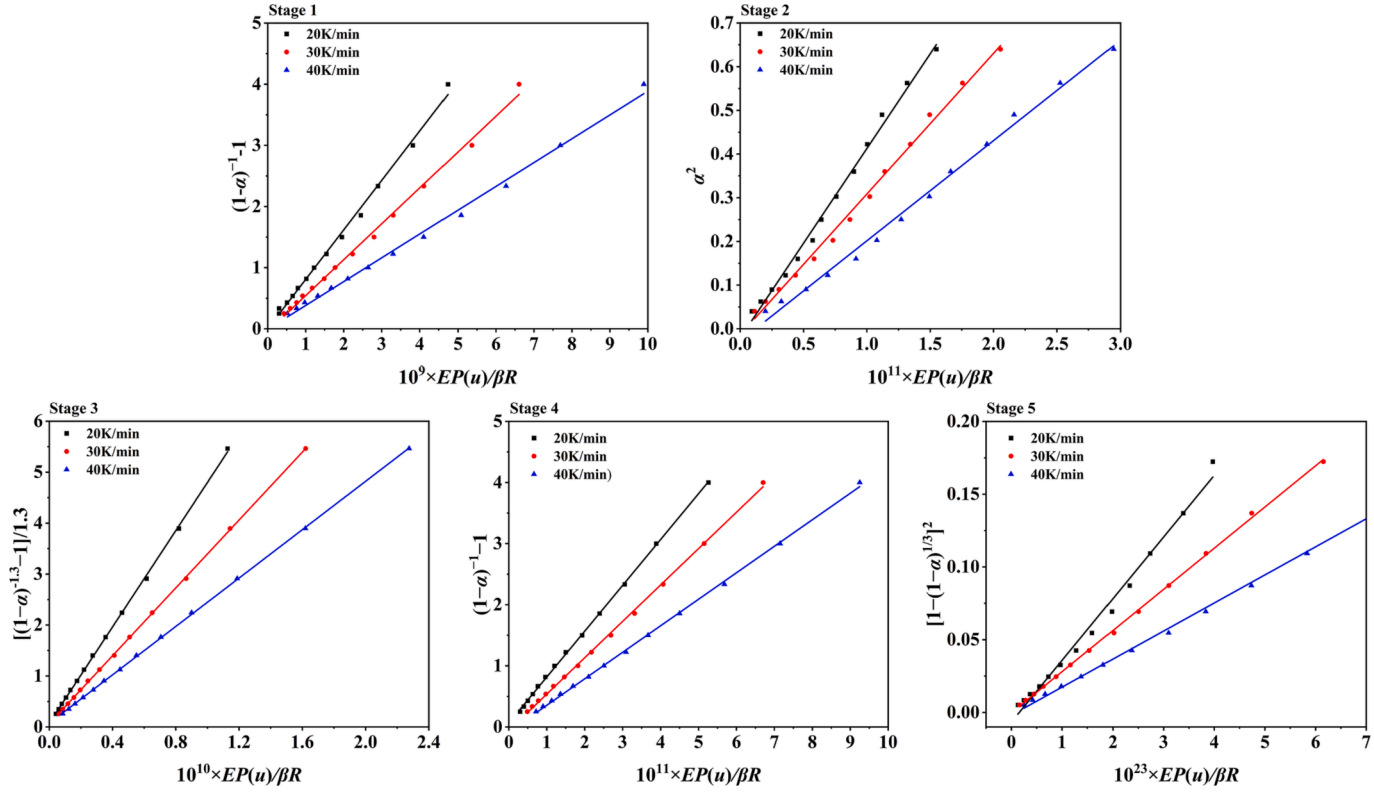

Fig. 4. Plotting $G(\alpha)$ versus 10x × $EP(u)/\beta R$ for the three sub-stages of DR pyrolysis.

to D1 of the theoretical master plots, which was a one-dimensional diffusion model of α^2. The three-dimensional diffusion (Jander) of D3 was the best-fit mechanism to describe the kinetics of the final sub-stage. Here, gaseous intermediates infiltrated the core of the initial material, forming a reaction layer that was then converted into the final products. Xie et al. [38] also reported that the major pyrolysis stages of antibiotic mycelial residue were described effectively by the three-dimensional diffusion. Meanwhile, the experimental master plot of Stage 3 was located between the theoretical master plots F2 and F3. The F_n model $f(\alpha) = (1-\alpha)^n$ could describe the kinetic process of Stage 3. Wang et al. [32] also found that reaction orders could effectively portray the decomposition of most organic matter, including proteins, carbohydrates, and aliphatic compounds in penicillin fermentation residues. Therefore, the expression $f(\alpha) = (1-\alpha)^n$ was introduced into Eq. (12) which became:

$$AG(\alpha) == \frac{AE}{\beta R} P(u_\alpha) = \frac{(1-a)^{1-n} - 1}{n-1} \tag{14}$$

To obtain the more appropriate value of n to express Stage 3, n was set to increase from 1.0 to 2.0 in 0.1 increments and $[(1-\alpha)^{1-n} - 1]/(n-1)$ was plotted versus $EP(u)/\beta R$ as a least-square regression line. As shown in Fig. 4, the fitted curve had the highest correlation coefficient when n = 1.3. The corresponding pre-exponential Factor A could be obtained from the slope of the fitted curve. The same method was used

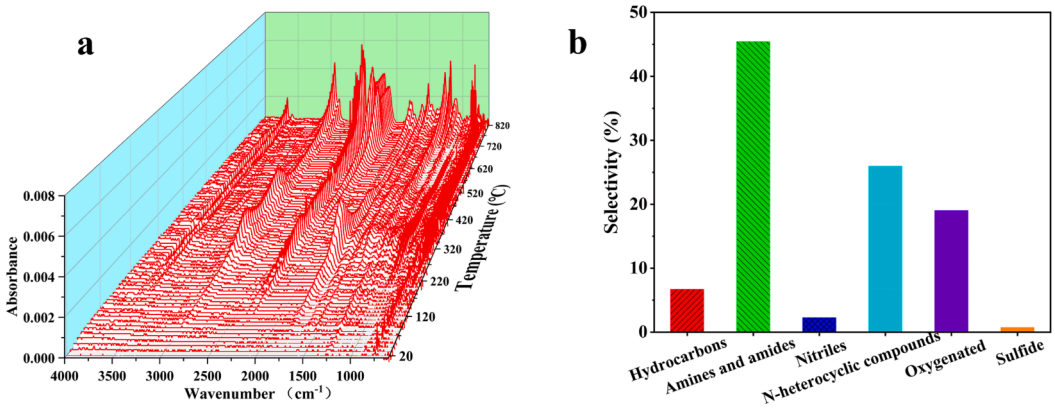

Fig. 5. (a): Three-dimensional infrared spectra of DR pyrolysis gases; (b): Relative peak area of classified bio-oil compounds from DR pyrolysis.

Table 3
Significant physicochemical properties of DR and DRCs.

Samples	Yield (%)	Proximate analysis (wt.%) on sample mass			Elementals analysis (wt.%) on sample mass							BET specific surfacearea ($m^2 \cdot g^{-1}$)
		Ash	VM	FC	N	C	H	S	O	H/C	N/C	
DR	/	48.05 ± 0.37	49.41 ± 0.47	2.54	3.49 ± 0.01	22.72 ± 0.05	3.22 ± 0.25	0.39 ± 0.01	22.13	1.70	0.13	3.76
DRC-400	65.97 ± 0.43	69.34 ± 0.13	26.42 ± 0.83	4.25	1.20 ± 0.08	13.01 ± 0.13	1.30 ± 0.38	0.41 ± 0.04	14.75	1.20	0.08	19.35
DRC-500	64.97 ± 0.24	70.27 ± 0.40	22.62 ± 0.08	7.11	1.27 ± 0.01	13.85 ± 0.01	1.25 ± 0.39	0.51 ± 0.08	12.85	1.08	0.08	38.38
DRC-600	62.27 ± 0.87	71.86 ± 0.28	19.45 ± 0.16	8.69	0.91 ± 0.04	13.28 ± 0.04	0.89 ± 0.03	0.52 ± 0.01	12.55	0.80	0.06	49.64
DRC-700	52.23 ± 0.56	81.71 ± 0.21	16.00 ± 0.03	2.29	0.34 ± 0.00	8.22 ± 0.01	1.09 ± 0.06	0.65 ± 0.16	8.00	1.59	0.04	93.98
DRC-800	51.57 ± 0.61	84.03 ± 0.17	13.48 ± 0.21	2.49	0.26 ± 0.00	7.71 ± 0.01	1.17 ± 0.23	0.52 ± 0.08	6.31	1.82	0.03	80.26

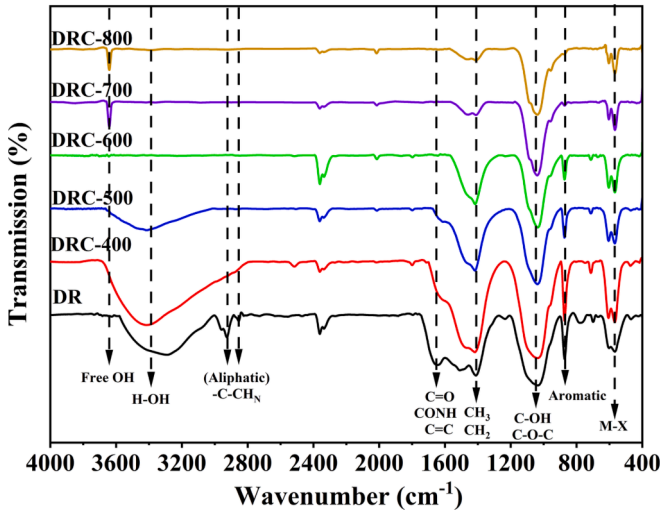

Fig. 6. FTIR spectra of DR and DRCs.

to obtain the kinetic triplets at 20 °C/min and 40 °C/min. The relevant results are presented in Table S3. The mechanism functions for the five sub-stages of DR pyrolysis were $f(\alpha) = (1-\alpha)^{-1} - 1$, $f(\alpha) = \alpha^2$, $f(\alpha) = [(1-\alpha)^{-1.3} - 1]/1.3$, $f(\alpha) = (1-\alpha)^{-1} - 1$, and $f(\alpha) = [1-(1-\alpha)^{1/3}]^2$, respectively.

3.4. TG-FTIR analyses and Py-GCMS analysis of pyrolysis oil

Fig. 5a shows the 3D infrared spectrum obtained using DR pyrolysis at 20 °C/min. The pyrolysis products of DR varied considerably with increasing pyrolysis temperature and were mainly concentrated between 250 and 800 °C. According to the Lambert–Beer law [39], the absorption spectra at specific wavelengths were linearly related to the gas concentration. Given that most of the gas spillover also falls within this range, the type of DR pyrolysis products could be determined from the FTIR profiles [40]. The absorption peaks around 3500–3700 cm^{-1} were mainly O-H and associated with the water adsorbed in DR. Part of this corresponded to the first stage of the process in thermogravimetric analysis. In contrast, the Maillard reaction (dehydration reaction) may generate the subsequent peaks, which corresponded to the third stage of DR pyrolysis. The absorption peaks neared 3000 cm^{-1} and were predominantly C-H of methane gas (CH_4). This was mainly associated with the cleavage of methoxy-O-CH_3 in hemicellulose, cellulose, and lignin. It increased in intensity with increasing pyrolysis temperature. This corresponded to the reaction in the three and fourth stage, which corresponds to the decomposition of cellulose, hemicellulose and lignin. The absorption peaks near 2250 cm^{-1} were mainly associated with the release of CO_2. This was caused by the cleavage recombination of acidic oxygen functional groups, such as carboxyl, lactones, and cleavage detachment of C–C and C–O linked to the main hemicellulose branch, the C═O cleavage of cellulose, and C–C breakage [41–43] (Mainly focused on the third stage). The significant increase in CO_2 after 670 °C is mainly related to the decomposition of calcium carbonate, which corresponds to the fifth stage of DR decomposition. The weak peaks between 600 and 800 °C were mainly secondary degradation of CO and CO compounds, leading to the reorganization of bond breaks. CO was detected near 2200–2300 cm^{-1}. The peak intensity increased with increasing pyrolysis temperature and was mainly generated by the reaction of C in DR with the generated CO_2 ($C + CO_2 \rightarrow 2CO$). In addition,

Table 4
Total concentrations of HMs on sample mass in DR and DRCs.

Sample	Heavy metals (mg/kg)							
	Cr	Mn	Ni	Cu	Zn	As	Cd	Pb
DR	35.31 ± 2.71	200.0 ± 19.0	12.42 ± 1.17	38.74 ± 1.29	264.5 ± 19.0	25.21 ± 2.61	1.097 ± 0.038	5.451 ± 0.190
DRC-400	44.93 ± 0.74	255.8 ± 4.0	15.91 ± 0.18	47.94 ± 1.46	349.2 ± 6.0	23.02 ± 0.12	1.600 ± 0.015	8.553 ± 0.254
DRC-500	41.92 ± 1.57	240.5 ± 6.0	15.33 ± 0.20	50.33 ± 0.58	336.4 ± 5.9	22.18 ± 0.25	1.309 ± 0.044	8.311 ± 0.097
DRC-600	42.67 ± 0.62	254.5 ± 5.9	15.83 ± 0.21	54.81 ± 1.05	317.8 ± 3.2	21.61 ± 0.55	0.146 ± 0.038	8.248 ± 0.392
DRC-700	44.91 ± 1.72	258.5 ± 15.2	16.61 ± 1.11	58.99 ± 3.39	204.3 ± 4.0	21.53 ± 0.87	0.027 ± 0.002	2.572 ± 0.193
DRC-800	42.98 ± 0.22	257.1 ± 1.6	16.11 ± 0.30	56.83 ± 0.37	119.1 ± 8.9	19.82 ± 0.56	0.021 ± 0.003	2.120 ± 0.127
Threshold [a]	500	–[b]	100	500	1200	30	3	30

[a] Threshold values given by the GB 4284-2018.
[b] Not listed.

part of CO is also derived from the decomposition of carbonyl groups and ethers in the DR. Carbon oxides are primarily formed from ether bridges connecting lignin subunits at lower temperatures and from the dissociation of diaryl ethers at higher temperatures [33]. The absorption peaks around 1700–1900 cm^{-1} corresponded to aldehydes, organic acids, and ketones produced by the cleavage of the epoxy group (–CH(O)CH–) [44], which mainly produced from the decomposition of hemicellulose and cellulose in the third stage. Meanwhile, 1500 ~ 1600 cm^{-1} were skeletal vibrations of C-C, that is, phenols with benzene ring groups and hydroxyl groups, which corresponded to the decomposition of cellulose and lignin in the fourth stage. Both the absorption peaks near 1300–1400 cm^{-1} and 1000–1200 cm^{-1} stretching vibrations were mainly because of hydroxyl (C(OH)) compounds, carbonyl groups, acids, ethers, phenols, and alcohols with the release of C═O, –OH and C–O(H) concentrated between 220 and 320 °C. In contrast, the absorption peaks below a wavelength of 1000 cm^{-1} were more often attributed to NH_3, mainly because of the generation of minor molecule gases from anaerobic digestate through deamidation reactions [45].

The Py-GCMS results indicated that the pyrolysis oil produced during DR pyrolysis was a highly complex mixture. The mass spectra were analyzed against the standard database, and peaks with areas corresponding to the weight percentage greater than 0.05% were recorded to obtain 56 compounds, as shown in Table S4 and Fig. 5b. The substances in pyrolysis oil were mainly classified as hydrocarbons, nitrogenous compounds, and oxygenated and sulphur compounds. The hydrocarbons in hydrocarbons mainly comprised olefins and PAHs. Olefins were primarily likely to be produced by the pyrolysis of lipids in the DR, while PAHs were mainly derived from secondary reactions of styrene derivatives such as phenol and cresol in pyrolytic volatiles [46]. Meanwhile, high levels of PAHs reduce fuel quality and are potentially harmful to the environment. However, the nitrogenous compounds mainly included amines and amides, nitrile, and nitrogen-containing heterocyclic compounds. Given the protein-rich nature of DR, over 73.59% of the pyrolysis products contained nitrogenous compounds. Of these, 45.41% were amines and amides, while the most dominant proportion was glycine at 44.42%. Amines and amides were mainly associated with the generation of methyl and methylene groups from amino acid dimerization in DR from meals and the reaction with fatty acids from lipolysis. The production of nitrile-like substances was mainly because of the cleavage reaction of amino acids and the dehydration reaction of amides. Among the nitrogen-containing heterocyclic compounds, indoles, pyridines, pyrroles, pyrazines, and piperidines were formed mainly because of dehydrogenation, decarboxylation, and dehydration of some amino acids. In contrast, the remaining pyridines and pyrroles were formed primarily because of secondary cleavage reactions of nitrogen-containing functional groups such as pyridine-N and pyrrole-N in cleaved carbon [47–49]. The Maillard reaction between carbonyl and amino compounds can produce nitrogen-containing heterocyclic compounds. In contrast, high nitrogen-containing compounds in pyrolysis oil can lead to nitrogen-related contamination. How effectively nitrogen-containing substances can be removed from the cracked oil can also affect the efficient application of subsequent products. The main oxygenated compound-like substances produced by DR pyrolysis were alcohols, aldehydes, ketones, acids, and phenols. The acids and ketones were mainly because of the degradation of hemicellulose. Meanwhile, phenols and aldehydes were caused more often by decomposition of lignin [50]. The sulphur compound contents were lower, at 0.71% and were mainly composed of sulphur-related acids, and ethers.

3.5. Characteristic analysis of DRCs

3.5.1. General properties

The biochar yield decreased with rising pyrolysis temperature (Table 3). This indicated that more volatile matter was released as liquids and gases. DR has higher quality than traditional sewage sludge, showing an advantage in terms of energy cycle self-sufficiency and lower carbon emissions. As the temperature increased, the ash content of the biochar rose from 48.05% to 84.03%. The volatile matter decreased from 49.41% to 13.48%, which was caused by massive decomposition of organic matter in the DR during pyrolysis. The high ash content of the biochar (81.71% at 700 °C and 84.03% at 800 °C) limits further use. The decreases in H and N contents at higher pyrolysis temperatures were because of the loss of more volatile matter. The S content of biochar was relatively constant despite the change in pyrolysis temperature. The molar ratios of H/C and O/C were the main carbonation parameters and have commonly been used to describe the organic aromaticity of biochar [51]. Both ratios (H/C) of the biochar declined significantly with increasing pyrolysis temperature, leading to substantially greater carbonization and higher aromatic condensation. The molar ratio of H/C decreased from 1.20 at 400 °C to 0.80 at 600 °C and then increased to 1.82 at 800 °C. This was consistent with the results for C content, indicating that the C content in biochar had dropped significantly at high temperatures of 700 and 800 °C. At high temperatures above 682 °C, the calcium carbonate in the DR decomposition produces a large amount of CO_2 overflow, therefore, reducing the C content, and the same O content also decreases (Table 3). The molar N/C ratio declined significantly with increasing pyrolysis temperature, suggesting a reduction in N-related functional groups on the biochar surface [52].

As shown in Table 3, as the pyrolysis temperature increased from 400 °C to 700 °C, the specific surface area of DR rose from 19.36 to 93.98 $m^2 \cdot g^{-1}$. However, when the pyrolysis temperature reached 800 °C, a slight downward trend in specific surface area was observed, decreasing to 80.26 $m^2 \cdot g^{-1}$. This can be attributed to the formation of calcium carbonate from the abundant organic calcification in DR under high-temperature pyrolysis conditions. This, in turn, decomposes into calcium oxide and CO_2 gaseous products spilling out of the solid phase, resulting in a rich pore structure [35]. The subsequent reduction was likely because of gradual melting of some of the low-melting fractions, with the liquid phase filling in the pores leading to a reduction in specific surface area.

3.5.2. FTIR analyses

The FTIR spectra of DR and DRCs are presented in Fig. 6. The specific stretching vibrations of –OH from mineral substances occurred at

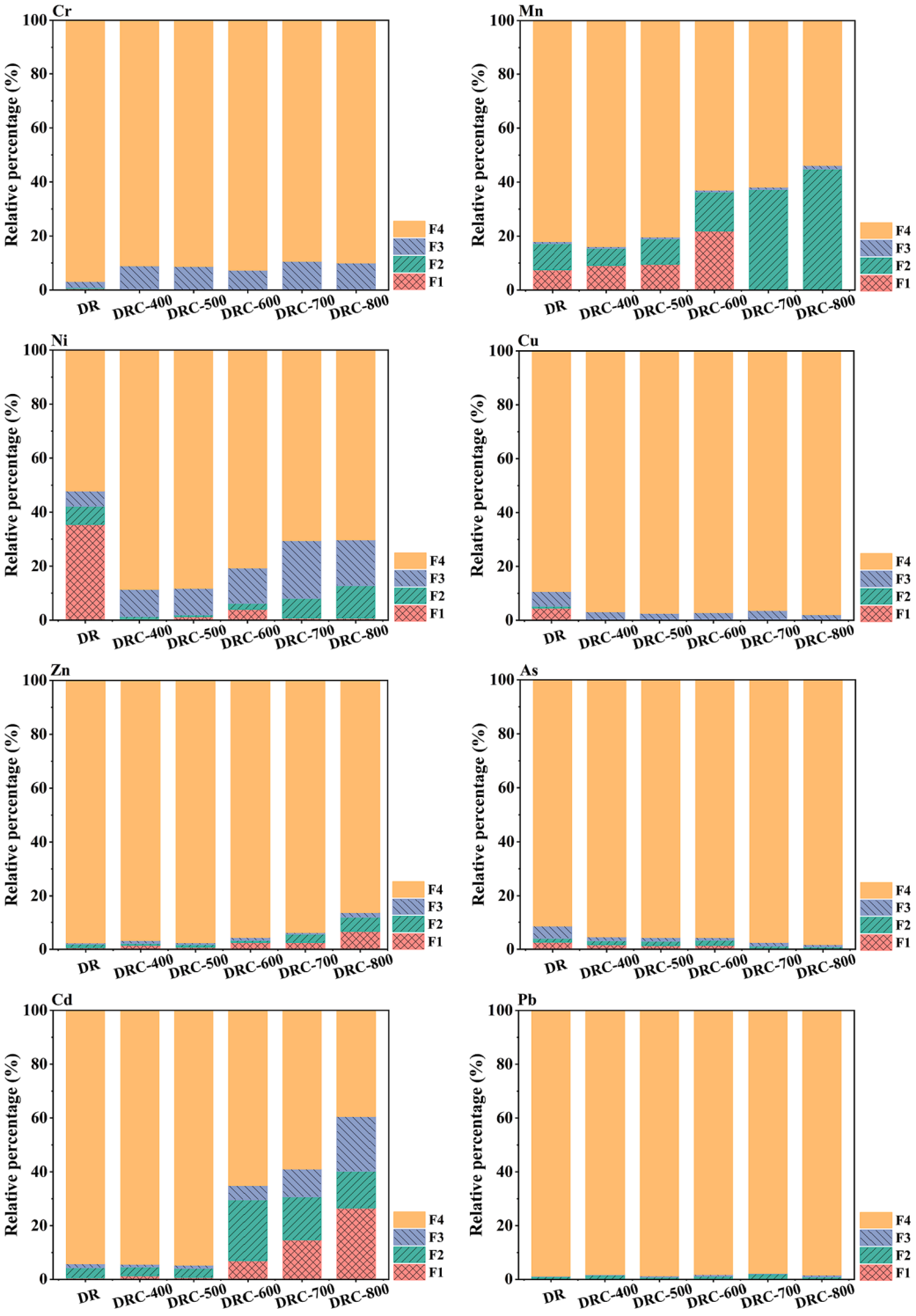

Fig. 7. BCR speciation of heavy metals in DR and DRCs.

approximately 3600 cm^{-1} and were only detectable at pyrolysis temperatures above 700 °C. The peak intensity near 3400 cm^{-1} was because of the hydroxyl functional group (vibration of O-H stretching). The tensile strength of O-H gradually weakened as the pyrolysis temperature rose and disappeared entirely under pyrolysis conditions higher than 600 °C. This indicated that the hydroxyl or carboxyl groups in the sugar units formed from the broken chains of cellulose and hemicellulose were completely decomposed after pyrolysis. The peak near 2800–3000 cm^{-1} was attributed to the aliphatic $(CH)_n$ group (C-H stretch), which weakened gradually as the pyrolysis temperature increased. This can be explained by organic fatty hydrocarbons being decomposed to carbon dioxide, methane, and other gases, or transformed into aromatic structures [53], which is also consistent with TG-FTIR results. The peak around 1601–1660 cm^{-1} reflected amide bonds and aromatic ring stretching (C═C, C═O and –CONH–), with a slight decrease in the intensity of the DRC as the temperature increases, and this could verify the formation of NH_3. Meanwhile, the peaks at 1417 and 1437 cm^{-1} were related to CH_3 and CH_2 aliphatic chains and decreased gradually with

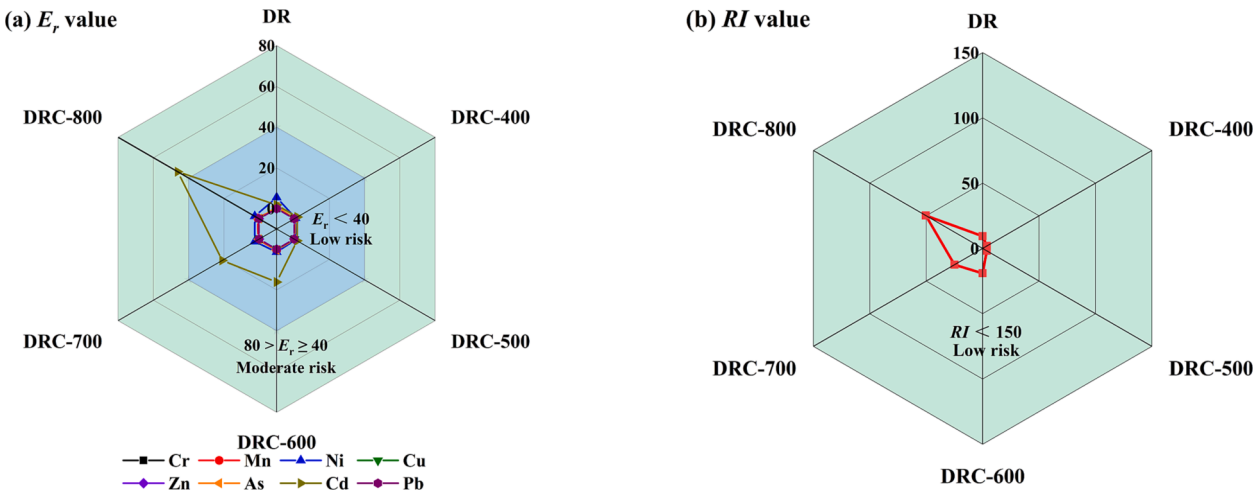

Fig. 8. (a) Single potential ecological risk indices (E_r) and (b) potential ecological risk indices (RI) of DR and DRCs. Different colored areas in the radar diagram indicate different risk levels.

increasing temperatures up to 800 °C. The peak around 1050 cm^{-1} attributed to aromatic C-O-C decreased slightly upon heating at higher pyrolysis temperature. This was related to the breakage of the aromatic C-O linkages and volatilization of oxygen corresponding to the formation of carbonyl groups, acids, ethers, phenols and alcohols in TG-FTIR in different compounds and poly-condensation of the aromatic structure [52].

3.6. HMs analysis

3.6.1. Total concentrations of HMs in DR and DRCs

The concentrations of Zn and Cu in DR were relatively high, reaching 264.5 mg/kg and 200.0 mg/kg, respectively (Table 4). However, the concentrations of Cd and Pb were low, at 1.097 mg/kg and 5.451 mg/kg, respectively. Except for As, there was a significant enrichment of DRCs prepared by pyrolysis at 400 and 500 °C. This increase can be attributed to the weight loss of HMs being substantially lower than that of the organic matter, which led to the enrichment of HMs in the carbon matrix [54]. Cr, Mn, Ni, Cu, and As concentrations in DRCs did not change substantially with increasing pyrolysis temperature. Meanwhile, Zn, Cd, and Pb showed a significant decrease in concern at temperatures up to 700 °C, with Zn decreasing further at 800 °C. The results can be attributed to the oxides of Cd and Pb being reduced by carbon to gas and overflowing in a high-temperature environment [55]. The main reason for the decrease in Zn concentration at high temperatures could be attributed to chemical reactions above 700 °C, culminating in migration from carbon to liquids and gases in the form of Zn or $ZnCl_2$ [56]. In summary, the DR and DR-derived biochar had safe HM concentrations, and met the Chinese control standards for contaminants in agricultural sludge (GB 4284–2018, A-level sludge, Cr: 500 mg/kg, Ni: 100 mg/kg, Cu: 500 mg/kg, Zn: 1200 mg/kg, As: 30 mg/kg, Cd: 3 mg/kg and Pb: 30 mg/kg).

3.6.2. Speciation of HMs in the DR and DRCs

Fig. 7 shows the variation in the chemical speciation of HMs in DR and DRCs. For Cr, Cu, and Pb, the percentages of F3 + F4 fractions in DR were relatively high, especially for Cr and Pb, at close to 100. The portions of those fractions remained at relatively high levels after pyrolysis, indicating a low environmental risk for Cu, Cr, and Pb in DR and DRCs. For Mn, Ni, Zn, and Cd, the percentages of F3 + F4 fractions all showed a tendency to decrease with increasing pyrolysis temperature. The percentage of the F3 + F4 fraction for Mn in DR increases from 82.73% to 84.47% at 400 °C and decreased to 55.07% when the temperature reached 800 °C. Meanwhile, the percentage of F3 + F4 fractions of Ni in DR increased from 57.73% to 98.56% in DR at 400 °C and decreased to 87.14% when the temperature increased to 800 °C. This may be because the high content of oxides and organic matter in the DR could be used to enhance interactions such as adsorption, precipitation, and complexation between the HMs and the lattice by increasing the negative charge. This immobilized the HMs in the high aromatic biochar structure [57,58]. However, under high-temperature conditions, some stable inorganic minerals in the DR, that is, mainly carbonates and silicates, decomposed during pyrolysis. This resulted in the release of fixed metals from the crystal structure [59]. The chloride in DR could significantly enhance the chlorination when it was pyrolyzed at temperatures above 700 °C, therefore, activating the HMs in biochar [60]. For As, the F4 fraction (91.31%) dominated in DR and showed a tendency to continue to increase in proportion with increasing pyrolysis temperature. This phenomenon may be because of the high content of calcium oxide in the DR. This has a strong inhibitory effect on As emission and can also react with As_2O_3, As_2S_3, and $NaAsO_2$ to form thermally stable compounds ($Ca(AsO_2)_2$) [61].

3.6.3. Assessment of potential ecological risks of DR and DRCs

The TCLP leaching amounts, which simulate the leaching of contaminants from landfills, provide a means of assessing the HMs risk of heavy metals. The leaching amounts of all HMs in DR and DRCs were less than the threshold values (Table S5). This indicated that the environmental risks were relatively low and would not cause contamination of the surrounding environment with HMs. Such low leaching amounts showed that DRCs potentially have a range of applications and have provided a basis for use as modified sorbent materials or soil fertilizers. Overall, pyrolysis was beneficial in further reducing the leaching of HMs and promoting the stabilization of HMs. This was also verified in the BCR spectral distribution analysis.

Potential ecological risk index (*RI*) results for HMs in DR and DRCs are shown in Fig. 8. The value of *RI* for the DR is 9.34, indicating that the contamination level of HMs is relatively low. The *RI* values showed a decreasing trend and then increased with increasing pyrolysis temperature, with a minimum of 3.65 when the pyrolysis temperature was 500 °C. The main reason for this increase was provided by the Cd mentioned in the BCR chemical specification analysis. Its E_r value was 46.23, which was a moderate risk of contamination. This is because Cd is present as metal chloride at high temperatures, increasing its hazard level. However, the lower concentrations make this less important.

4. Conclusion

The pyrolytic properties, mechanism of product formation, biochar characteristics, and heavy metals safety of biochar during the pyrolysis of food waste digestate residues have been examined in the current study. The results have shown that DR pyrolysis proceeded in five stages. The kinetic model for Stage 1, Stage 3, and Stage 4 were the simple reaction order model, the one-dimensional diffusion model for Stage 2, and the three-dimensional (Jander) diffusion model for Stage 5. Based on the TG-FTIR and Py-GCMS analysis, the volatile components of DR pyrolysis were mainly generated through the Maillard, decarboxylation, and deamination reactions as H_2O, CH_4, CO_2, CO, phenol, C═O (anhydride, ketone or aldehyde), C-O, and NH_3. Meanwhile, the main components of the pyrolysis oil were of six types, that is, hydrocarbons, amines and amides, nitrile, N-hybrid compounds, oxides, and sulphides, of which glutamate had the largest proportion of 44.42%. The prepared DRCs had suitable aromatic properties. The biochar obtained at a pyrolysis temperature of 700 °C has a relatively high specific surface area. The HMs results have shown that the HMs of DRCs from DR pyrolysis at 400, 500, 600, 700, and 800 °C were mainly in the F3 and F4 fractions. TCLP leaching toxicity tests and heavy metal potential ecological risk indices have indicated a high safety profile for DRCs. Moreover, we have successfully applied DRCs in adsorption with promising results [62].

CRediT authorship contribution statement

Yu Wang: Writing – original draft, Visualization, Formal analysis, Data curation, Conceptualization. **Guangwei Yu:** Writing – review & editing, Supervision, Project administration, Conceptualization. **Shengyu Xie:** Writing – review & editing. **Ruqing Jiang:** Writing – review & editing. **Changjiang Li:** Data curation. **Zhenjiao Xing:** Data curation.

Declaration of Competing Interest

The authors declare that they have no known competing financial interests or personal relationships that could have appeared to influence the work reported in this paper.

Data availability

Data will be made available on request.

Acknowledgements

All the authors are thankful for the support provided by the National Key Research and Development Project (2020YFC1908904) and the Science and Technology Project of Fujian Province (2021T3069, 3502ZCQXT2022004).

Appendix A. Supplementary data

Supplementary data to this article can be found online at https://doi.org/10.1016/j.fuel.2023.129185.

References

[1] Jin C, Sun S, Yang D, Sheng W, Ma Y, He W, et al. Anaerobic digestion: An alternative resource treatment option for food waste in China. Sci Total Environ 2021;779:146397.
[2] Posmanik R, Labatut RA, Kim AH, Usack JG, Tester JW, Angenent LT. Coupling hydrothermal liquefaction and anaerobic digestion for energy valorization from model biomass feedstocks. Bioresour Technol 2017;233:134–43.
[3] Xu FQ, Li YY, Ge XM, Yang LC, Li YB. Anaerobic digestion of food waste – Challenges and opportunities. Bioresour Technol 2018;247:1047–58.
[4] Romero-Güiza MS, Vila J, Mata-Alvarez J, Chimenos JM, Astals S. The role of additives on anaerobic digestion: A review. Renew Sustain Energy Rev 2016;58:1486–99.
[5] Li Y, Chen Y, Wu J. Enhancement of methane production in anaerobic digestion process: A review. Appl Energy 2019;240:120–37.
[6] Li YY, Jin YY, Borrion A, Li HL. Current status of food waste generation and management in China. Bioresour Technol 2019;273:654–65.
[7] Xu FQ, Shi J, Lv W, Yu ZT, Li YB. Comparison of different liquid anaerobic digestion effluents as inocula and nitrogen sources for solid-state batch anaerobic digestion of corn stover. Waste Manag 2013;33(1):26–32.
[8] Wang Y, Yu GW, Lin JJ, Li CJ, Jiang RQ, Xing ZJ, et al. Preparation of building ceramsite from food waste digestate residues, incineration fly ash and sludge biochar. Chem Ind Eng Progress 2022. 10.16085/j.issn.1000-6613.2022-0664.
[9] Opatokun SA, Strezov V, Kan T. Product based evaluation of pyrolysis of food waste and its digestate. Energy 2015;92:349–54.
[10] Wojnowska-Baryła I, Bernat K, Sartowska S. Biological stability of multi-component agri-food digestates and post-digestates. Waste Manag 2018;77:140–6.
[11] Manu MK, Li D, Liwen L, Jun Z, Varjani S, Wong JWC. A review on nitrogen dynamics and mitigation strategies of food waste digestate composting. Bioresour Technol 2021;334:125032.
[12] Tyagi VK, Fdez-Güelfo LA, Zhou Y, Álvarez-Gallego CJ, Garcia LIR, Ng WJ. Anaerobic co-digestion of organic fraction of municipal solid waste (OFMSW): Progress and challenges. Renew Sustain Energy Rev 2018;93:380–99.
[13] He M, Cao Y, Xu Z, You S, Ruan R, Gao B, et al. Process water recirculation for catalytic hydrothermal carbonization of anaerobic digestate: Water-Energy-Nutrient Nexus. Bioresour Technol 2022;361:127694.
[14] Dutta S, He M, Xiong X, Tsang DCW. Sustainable management and recycling of food waste anaerobic digestate: A review. Bioresour Technol 2021;341:125915.
[15] Lu J, Xu S. Post-treatment of food waste digestate towards land application: A review. J Clean Prod 2021;303:127033.
[16] Herbes C, Roth U, Wulf S, Dahlin J. Economic assessment of different biogas digestate processing technologies: A scenario-based analysis. J Clean Prod 2020;255:120282.
[17] Wang T-T, Wang S-P, Zhong X-Z, Sun Z-Y, Huang Y-L, Tan LI, et al. Converting digested residue eluted from dry anaerobic digestion of distilled grain waste into value-added fertilizer by aerobic composting. J Clean Prod 2017;166:530–6.
[18] Grigatti M, Barbanti L, Hassan MU, Ciavatta C. Fertilizing potential and CO2 emissions following the utilization of fresh and composted food-waste anaerobic digestates. Sci Total Environ 2020;698:134198.
[19] Vyazovkin S, Chrissafis K, Di Lorenzo ML, Koga N, Pijolat M, Roduit B, et al. ICTAC Kinetics Committee recommendations for collecting experimental thermal analysis data for kinetic computations. Thermochim Acta 2014;590:1–23.
[20] Lin Y, Ma X, Yu Z, Cao Y. Investigation on thermochemical behavior of co-pyrolysis between oil-palm solid wastes and paper sludge. Bioresour Technol 2014;166:444–50.
[21] Mishra G, Bhaskar T. Non isothermal model free kinetics for pyrolysis of rice straw. Bioresour Technol 2014;169:614–21.
[22] Flynn JH, Wall LA. A quick, direct method for the determination of activation energy from thermogravimetric data. J Polym Sci, Part C: Polym Lett 1966;4(5):323–8.
[23] Fang S, Yu Z, Lin Y, Lin Y, Fan Y, Liao Y, et al. Effects of additives on the co-pyrolysis of municipal solid waste and paper sludge by using thermogravimetric analysis. Bioresour Technol 2016;209:265–72.
[24] Chen CX, Ma XQ, He Y. Co-pyrolysis characteristics of microalgae Chlorella vulgaris and coal through TGA. Bioresour Technol 2012;117:264–73.
[25] Chen J, Mu L, Jiang B, Yin H, Song X, Li A. TG/DSC-FTIR and Py-GC investigation on pyrolysis characteristics of petrochemical wastewater sludge. Bioresour Technol 2015;192:1–10.
[26] Vyazovkin S, Burnham AK, Criado JM, Pérez-Maqueda LA, Popescu C, Sbirrazzuoli N. ICTAC Kinetics Committee recommendations for performing kinetic computations on thermal analysis data. Thermochim Acta 2011;520(1):1–19.
[27] Wang Y, Yu GW, Jiang RQ, Lin JJ, Wang Y. Effect of particle size on phosphorus and heavy metals during the preparation of biochar from food waste biogas residue. CIESC J 2021;72(10):5344–53.
[28] Hakanson L. An ecological risk index for aquatic pollution control.a sedimentological approach. Water Res 1980;14(8):975–1001.
[29] Wang Yu, Yu G, Lin J, Jiang R, Xu X, Xie S, et al. Synergistic hydrothermal treatment of food waste digestate residues and incineration fly ash: dehydration performance and heavy metals safety. React Chem Eng 2022;7(8):1797–806.
[30] Hu M, Chen Z, Guo D, Liu C, Xiao Bo, Hu Z, et al. Thermogravimetric study on pyrolysis kinetics of Chlorella pyrenoidosa and bloom-forming cyanobacteria. Bioresour Technol 2015;177:41–50.
[31] Zong P, Jiang Y, Tian Y, Li J, Yuan M, Ji Y, et al. Pyrolysis behavior and product distributions of biomass six group components: Starch, cellulose, hemicellulose, lignin, protein and oil. Energ Conver Manage 2020;216:112777.
[32] Wang Z, Hong C, Xing Yi, Li Z, Li Y, Yang J, et al. Thermal characteristics and product formation mechanism during pyrolysis of penicillin fermentation residue. Bioresour Technol 2019;277:46–54.
[33] Gu XL, Ma X, Li LX, Liu C, Cheng KH, Li ZZ. Pyrolysis of poplar wood sawdust by TG-FTIR and Py–GC/MS. J Anal Appl Pyrol 2013;102:16–23.
[34] Karunadasa KSP, Manoratne CH, Pitawala HMTGA, Rajapakse RMG. Thermal decomposition of calcium carbonate (calcite polymorph) as examined by in-situ high-temperature X-ray powder diffraction. J Phys Chem Solid 2019;134:21–8.
[35] Liu J, Huang S, Chen K, Wang T, Mei M, Li J. Preparation of biochar from food waste digestate: Pyrolysis behavior and product properties. Bioresour Technol 2020;302:122841.
[36] Zou J, Hu H, Rahman MM, Yellezuome D, He F, Zhang X, et al. Non-isothermal pyrolysis of xylan, cellulose and lignin: A hybrid simulated annealing algorithm and pattern search method to regulate distributed activation energies. Ind Crop Prod 2022;187:115501.

[37] Cai HM, Liu JY, Xie WM, Kuo JH, Buyukada M, Evrendilek F. Pyrolytic kinetics, reaction mechanisms and products of waste tea via TG-FTIR and Py-GC/MS. Energ Conver Manage 2019;184:436–47.
[38] Xie S, Wang Yu, Ma C, Zhu G, Wang Y, Li C. Pyrolysis of antibiotic mycelial residue for biochar: Kinetic deconvolution, biochar properties, and heavy metal immobilization. J Environ Manage 2023;328:116956.
[39] Chen H, Xie Y, Chen W, Xia M, Li K, Chen Z, et al. Investigation on co-pyrolysis of lignocellulosic biomass and amino acids using TG-FTIR and Py-GC/MS. Energ Conver Manage 2019;196:320–9.
[40] Carangelo RM, Solomon PR, Gerson DJ. Application of TG-FT-i.r. to study hydrocarbon structure and kinetics. Fuel 1987;66(7):960–7.
[41] Sajjadi B, Zubatiuk T, Leszczynska D, Leszczynski J, Chen WY. Chemical activation of biochar for energy and environmental applications: a comprehensive review. 2019;35(7):777-815.
[42] Ding YM, Ezekoye OA, Lu SX, Wang CJ. Thermal degradation of beech wood with thermogravimetry/Fourier transform infrared analysis. Energ Conver Manage 2016;120:370–7.
[43] Figueiredo JL, Pereira MFR, Freitas MMA, Órfão JJM. Modification of the surface chemistry of activated carbons. Carbon 1999;37(9):1379–89.
[44] Zhang Z, Wang CJ, Huang G, Liu HR, Yang SL, Zhang AF. Thermal degradation behaviors and reaction mechanism of carbon fibre-epoxy composite from hydrogen tank by TG-FTIR. J Hazard Mater 2018;357:73–80.
[45] Li J, Liu YW, Shi JY, Wang ZY, Hu L, Yang X, et al. The investigation of thermal decomposition pathways of phenylalanine and tyrosine by TG–FTIR. Thermochim Acta 2008;467(1):20–9.
[46] Dai Q, Jiang X, Jiang Y, Jin Y, Wang F, Chi Y, et al. Formation of PAHs during the pyrolysis of dry sewage sludge. Fuel 2014;130:92–9.
[47] Tian K, Liu WJ, Qian TT, Jiang H, Yu HQ. Investigation on the Evolution of N-Containing Organic Compounds during Pyrolysis of Sewage Sludge. Environ Sci Tech 2014;48(18):10888–96.
[48] Lorenzetti C, Conti R, Fabbri D, Yanik J. A comparative study on the catalytic effect of H-ZSM5 on upgrading of pyrolysis vapors derived from lignocellulosic and proteinaceous biomass. Fuel 2016;166:446–52.
[49] Debono O, Villot A. Nitrogen products and reaction pathway of nitrogen compounds during the pyrolysis of various organic wastes. J Anal Appl Pyrol 2015; 114:222–34.
[50] Chen WH, Wang CW, Kumar G, Rousset P, Hsieh TH. Effect of torrefaction pretreatment on the pyrolysis of rubber wood sawdust analyzed by Py-GC/MS. Bioresour Technol 2018;259:469–73.
[51] Cayuela ML, Jeffery S, van Zwieten L. The molar H: Corg ratio of biochar is a key factor in mitigating N2O emissions from soil. Agr Ecosyst Environ 2015;202:135–8.
[52] Jin J, Li Y, Zhang J, Wu S, Cao Y, Liang P, et al. Influence of pyrolysis temperature on properties and environmental safety of heavy metals in biochars derived from municipal sewage sludge. J Hazard Mater 2016;320:417–26.
[53] Lu HL, Zhang WH, Wang SZ, Zhuang LW, Yang YX, Qiu RL. Characterization of sewage sludge-derived biochars from different feedstocks and pyrolysis temperatures. J Anal Appl Pyrol 2013;102:137–43.
[54] Xie S, Yu G, Li C, Li J, Wang G, Dai S, et al. Treatment of high-ash industrial sludge for producing improved char with low heavy metal toxicity. J Anal Appl Pyrol 2020;150:104866.
[55] Zhang ZY, Ju R, Zhou HT, Chen HW. Migration characteristics of heavy metals during sludge pyrolysis. Waste Manag 2021;120:25–32.
[56] Wang JC, Yang LN, Ko JH, Qi-Yong XU. Study on heavy metals in particulate matter of municipal sewage sludge pyrolysis. China Environ Sci 2018;38(10): 3781–7.
[57] Shi W, Liu C, Ding D, Lei Z, Yang Y, Feng C, et al. Immobilization of heavy metals in sewage sludge by using subcritical water technology. Bioresour Technol 2013;137: 18–24.
[58] Shao J, Yuan X, Leng L, Huang H, Jiang L, Wang H, et al. The comparison of the migration and transformation behavior of heavy metals during pyrolysis and liquefaction of municipal sewage sludge, paper mill sludge, and slaughterhouse sludge. Bioresour Technol 2015;198:16–22.
[59] Li ZJ, Deng H, Yang L, Zhang GL, Li YQ, Ren YS. Influence of potassium hydroxide activation on characteristics and environmental risk of heavy metals in chars derived from municipal sewage sludge. Bioresour Technol 2018;256:216–23.
[60] Xia Y, Tang Y, Shih K, Li B. Enhanced phosphorus availability and heavy metal removal by chlorination during sewage sludge pyrolysis. J Hazard Mater 2020;382: 121110.
[61] Han H, Hu S, Lu C, Wang Yi, Jiang L, Xiang J, et al. Inhibitory effects of CaO/Fe2O3 on arsenic emission during sewage sludge pyrolysis. Bioresour Technol 2016;218:134–9.
[62] Wang Y, Yu GW, Jiang RQ, Li CJ, Lin J, Xing ZJ. Study on the adsorption of ciprofloxacin hydrochloride by biochar from food waste digestate residues. Chem Ind Eng Progress 2022. 10.16085/j.issn.1000-6613.2022-1152.